Unsteadiness in the wake of disks and spheres: Instability, receptivity and control using direct and adjoint global stability analyses

P. Meliga[a,b,*], J.-M. Chomaz[b], D. Sipp[a]

[a]*ONERA/DAFE, 92190 Meudon, France*
[b]*LadHyX, CNRS-Ecole Polytechnique, 91128 Palaiseau, France*

Abstract

We consider the stability of the steady, axisymmetric wake of a disk and a sphere as a function of the Reynolds number. Both the direct and adjoint eigenvalue problems are solved. The threshold Reynolds numbers and characteristics of the destabilizing modes agree with that documented in previous studies: for both configurations, the first destabilization occurs for a stationary mode of azimuthal wavenumber $m = 1$, and the second destabilization for an oscillating mode of same azimuthal wavenumber. For both geometries, the adjoint mode computation allows us to determine the receptivity of each mode to particular initial conditions or forcing and to define control strategies. We show that the adjoint global mode reaches a maximum amplitude within the recirculating bubble and downstream of the separation point for both the disk and the sphere. In the case of the sphere, the optimal forcing corresponds to a displacement of the separation point along the sphere surface with no tilt of the separation line. However, in the case of the disk, its blunt shape does not allow such displacement and the optimal forcing corresponds to a tilt of the separation line with no displacement of the separation point. As a result, the magnitudes of the adjoint global modes are larger for the sphere than for the disk, showing that the wake of the sphere is more receptive to forcing than the disk. In the case of active control at the boundary through blowing and suction at the body wall, the actuator should be placed close to the separation point, where the magnitude of the adjoint pressure reaches its maximum in the four cases. In the case of passive control, we show that the region of the wake that is most sensitive to local modifications of the linearized Navier–Stokes operator, including base flow alterations, is limited to the recirculating bubble for both geometries and both instability modes. This region may therefore be identified as the intrinsical wavemaker.

*Corresponding author at: LadHyX, CNRS-Ecole Polytechnique, 91128 Palaiseau, France. Tel.: +33 1 69 33 52 73; fax: +33 1 69 33 52 92.

E-mail address: philippe.meliga@ladhyx.polytechnique.fr (P. Meliga).

1. Introduction

A large body of work has been devoted to the wake of axisymmetric bodies in the last decades. For different objects, such as spheres, disks or bullet-shaped bodies (Achenbach, 1974; Fuchs et al., 1979; Berger et al., 1990; Sevilla and Martínez-Bazàn, 2004), the dynamics bears similarities: at low Reynolds numbers, the steady separated flow field is axisymmetric and consists of a toroidal recirculation eddy past the body. Increasing the Reynolds number, a stationary bifurcation first occurs and breaks the axisymmetry, the entire wake being shifted in one direction. The series of bifurcation that follows is complex and body-shape dependent (Fabre et al., 2008), but eventually, for large enough Reynolds numbers, the flow is dominated by helical modes of azimuthal wavenumbers $m = \pm 1$, resulting in the low frequency shedding of large-scale coherent structures. These vortex shedding phenomena are characterized by low Strouhal numbers based on the body diameter, of order $0.1-0.2$.

Natarajan and Acrivos (1993) have carried out a global stability analysis of the axisymmetric wake past a circular flat disk set normal to the flow and a sphere. In both cases, they have shown that the axisymmetric base flow presents several successive destabilizations. The first instability is stationary and involves a global eigenmode of azimuthal wavenumber $m = 1$. The associated bifurcation, breaking the axisymmetry but preserving the time invariance, leads to a 3-D steady state. Above the threshold of instability, these authors have not studied the stability of this 3-D state but that of the axisymmetric wake. They have shown that a second instability occurs at a larger Reynolds number, for $m = \pm 1$ oscillating global eigenmodes that breaks the time invariance. From direct numerical simulations (DNS) and experimental observations, it turns out that this second instability mode dominates the dynamics of the fully 3-D flow at large Reynolds numbers, hence explaining the occurrence of a fully 3-D periodic state (Ormières and Provansal, 1998). Such a domination of the periodic instability mode, over the stationary mode, despite the fact that the latter is the first to destabilize the axisymmetric base flow has recently been explained using slow manifold theory and normal forms (Fabre et al., 2008). To be more specific, the sequence of bifurcations undergone by the real flow involves the destabilization of the steady tridimensional branch by an antisymmetric or a symmetric perturbation made of the superposition of two counter-rotating oscillating modes with different phases. In the case of the sphere, this second bifurcation has also been studied by Pier (2008) using the concepts of convective and absolute instability. His finding that the most absolutely unstable mode is symmetric is consistent with the symmetry properties of the solution after the threshold of instability (Fabre et al., 2008; Gumowski et al., 2008). However, this competition between modes is not the scope of the present study that focuses instead on the respective sensitivity and receptivity properties of these unstable global modes in two model geometries of blunt and bluff bodies, namely the disk and the sphere.

This study extends the work of Natarajan and Acrivos (1993) by carrying out an adjoint analysis of the wake past a circular flat disk and a sphere. We compute the direct and adjoint global modes associated to the first two instabilities. We discuss the non-normality of the flow and point out the role of the so-called *convective* non-normality (Chomaz et al., 1990; Chomaz, 2005; Marquet et al., 2009) associated to the transport of the perturbations by the base flow. The paper is organized as follows. The problems of direct and adjoint global modes are presented in Section 2, where we discuss the physical origin of the non-normality of the linearized Navier–Stokes equations. Section 3 presents the numerical method and the results of the direct and adjoint global stability analysis. We finally discuss physical interpretations of the adjoint global mode in terms of receptivity of the global mode to initial perturbations and forcing and, following Giannetti and Luchini (2007), we identify the 'wavemaker' region as the region of the flow where the instability is sensitive to local modification of the linearized evolution operator. These properties are crucial when control or, for instance, departure from the ideal axisymmetry owing to imperfect experimental set-ups are concerned.

2. Problem formulation

We investigate the stability of the axisymmetric flow developing past an axisymmetric body, that can be a flat circular disk normal to the incoming flow, or a sphere. Standard cylindrical coordinates r, θ and z with origin taken at the centre of the body are used. The configuration is shown in Fig. 1 for the flow past a sphere. The body of boundary $\partial\Omega_{\mathrm{bod}}$ is located on the axis of an enclosing cylinder of radius $r_\infty = 25$ defining the computational domain Ω, with boundaries $\partial\Omega_{\mathrm{ax}}$ and $\partial\Omega_{\mathrm{ext}}$ representing, respectively, the revolution axis of the base flow and the boundary of the enclosing cylinder. The inlet $\partial\Omega_{\mathrm{in}}$ and outlet $\partial\Omega_{\mathrm{out}}$ are located, respectively, at $z_{-\infty} = -100$ and $z_\infty = 200$.

All quantities are made non-dimensional using the diameter of the body D and the free-stream velocity U_∞. The state vector $\boldsymbol{q}$ stands for the flow field $(\boldsymbol{u}, p)^{\mathrm{T}}$, where superscript $^{\mathrm{T}}$ designates the transpose, $\boldsymbol{u} = (u, v, w)^{\mathrm{T}}$ is the fluid velocity where u, v and w are the radial, azimuthal and streamwise components, and p is the pressure. The fluid motion is
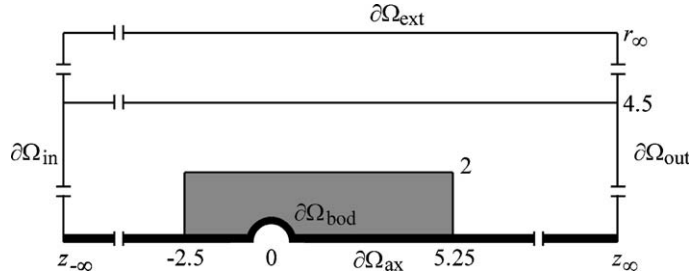
Fig. 1. Schematic of the mesh structure: $z_{-\infty}$, z_∞ and r_∞ are, respectively, the location of the inlet, outlet and external boundaries. The inner solid lines delimit regions characterized by different vertex densities. The grey shaded area corresponds to the region of highest density.

governed by the incompressible Navier–Stokes equations that read

$$\boldsymbol{\nabla} \cdot \boldsymbol{u} = 0, \quad \partial_t \boldsymbol{u} + \boldsymbol{\nabla}\boldsymbol{u} \cdot \boldsymbol{u} + \boldsymbol{\nabla}p - \frac{1}{\mathrm{Re}}\boldsymbol{\nabla}^2\boldsymbol{u} = \boldsymbol{0}, \tag{1}$$

where Re is the Reynolds number based on D and U_∞. We use the inlet condition $\boldsymbol{u} = (0,0,1)^{\mathrm{T}}$ on $\partial\Omega_{\mathrm{in}}$, no-slip conditions $\boldsymbol{u} = \boldsymbol{0}$ on the body wall $\partial\Omega_{\mathrm{bod}}$ and no-stress conditions $-p\boldsymbol{n} + \mathrm{Re}^{-1}\boldsymbol{\nabla}\boldsymbol{u} \cdot \boldsymbol{n} = \boldsymbol{0}$ on the outlet $\partial\Omega_{\mathrm{out}}$. On the external boundary $\partial\Omega_{\mathrm{ext}}$, we impose a free slip boundary condition $u = v = \partial_r w = 0$, so that the body surface $\partial\Omega_{\mathrm{bod}}$ is the only source of vorticity, as it would be the case without this artificial boundary.

2.1. Base flow

For Reynolds numbers below the threshold of the first instability, the flow can be searched as a steady, axisymmetric solution $\boldsymbol{q^0} = (u^0, 0, w^0, p^0)^{\mathrm{T}}$ satisfying

$$\boldsymbol{\nabla} \cdot \boldsymbol{u^0} = 0, \quad \boldsymbol{\nabla}\boldsymbol{u^0} \cdot \boldsymbol{u^0} + \boldsymbol{\nabla}p^0 - \frac{1}{\mathrm{Re}}\boldsymbol{\nabla}^2\boldsymbol{u^0} = \boldsymbol{0}. \tag{2}$$

On the axis $\partial\Omega_{\mathrm{ax}}$, we impose $u^0 = \partial_r w^0 = 0$, a condition given by mass and momentum conservation as $r \to 0$ for axisymmetric solutions.

2.2. Global mode analysis

The stability of the steady axisymmetric base flow is examined by considering small-amplitude 3-D perturbations $\boldsymbol{q^1} = (u^1, v^1, w^1, p^1)^{\mathrm{T}}$ which satisfy the unsteady equations linearized about $\boldsymbol{q^0}$

$$\boldsymbol{\nabla} \cdot \boldsymbol{u^1} = 0, \quad \partial_t \boldsymbol{u^1} + \mathscr{C}(\boldsymbol{u^1}, \boldsymbol{u^0}) + \boldsymbol{\nabla}p^1 - \frac{1}{\mathrm{Re}}\boldsymbol{\nabla}^2\boldsymbol{u^1} = \boldsymbol{0}, \tag{3}$$

where $\mathscr{C}(\boldsymbol{a}, \boldsymbol{b}) = \boldsymbol{\nabla}\boldsymbol{a} \cdot \boldsymbol{b} + \boldsymbol{\nabla}\boldsymbol{b} \cdot \boldsymbol{a}$ is the advection operator. Note that $\mathscr{C}$ is symmetrical, i.e. $\mathscr{C}(\boldsymbol{a}, \boldsymbol{b}) = \mathscr{C}(\boldsymbol{b}, \boldsymbol{a})$. When considering the perturbation and base flow velocity fields $\boldsymbol{u^1}$ and $\boldsymbol{u^0}$, this operator accounts for the advection of the perturbation by the base flow via the term $\boldsymbol{\nabla}\boldsymbol{u^1} \cdot \boldsymbol{u^0}$ and for the advection of the base flow by the perturbation via the term $\boldsymbol{\nabla}\boldsymbol{u^0} \cdot \boldsymbol{u^1}$. Since the base flow is axisymmetric, all perturbations are chosen in the form of normal eigenmodes of azimuthal wavenumber m and complex pulsation $\sigma + i\omega$, σ and ω being, respectively, the growth rate and pulsation of the eigenmode ($\sigma > 0$ for an unstable eigenmode):

$$\boldsymbol{q^1} = \hat{\boldsymbol{q}}^1(r, z)\mathrm{e}^{(\sigma + i\omega)t + im\theta} + \mathrm{c.c.}, \tag{4}$$

where $\hat{\boldsymbol{q}}^1 = (\hat{u}^1, \hat{v}^1, \hat{w}^1, \hat{p}^1)^{\mathrm{T}}$ is the so-called global mode, herein referred to as the *direct* global mode, for which both the cross-stream and streamwise directions (r, z) are eigendirections. Substitution of decomposition (4) in Eqs. (3) leads to a generalized eigenvalue problem for $\sigma + i\omega$ and $\hat{\boldsymbol{q}}^1$ that reads

$$(\sigma + i\omega)\mathscr{B}\hat{\boldsymbol{q}}^1 + \mathscr{A}_m\hat{\boldsymbol{q}}^1 = \boldsymbol{0}, \tag{5}$$

where $\mathscr{A}_m$ and $\mathscr{B}$ are the linear operators defined by

$$\mathscr{A}_m = \begin{pmatrix} \mathscr{C}_m(\cdot, \boldsymbol{u^0}) - \dfrac{1}{\mathrm{Re}}\boldsymbol{\nabla}_m^2 & \boldsymbol{\nabla}_m \\ \boldsymbol{\nabla}_m^{\mathrm{T}} & 0 \end{pmatrix}, \quad \mathscr{B} = \begin{pmatrix} \mathscr{I} & 0 \\ 0 & 0 \end{pmatrix}. \tag{6}$$

For a normal mode $\hat{\boldsymbol{a}}$ of azimuthal wavenumber m, the gradient operator and the velocity gradient tensor read

$$\boldsymbol{\nabla}_m = \begin{pmatrix} \partial_r \\ \dfrac{im}{r} \\ \partial_z \end{pmatrix}, \quad \boldsymbol{\nabla}_m\hat{\boldsymbol{a}} = \begin{pmatrix} \partial_r \hat{u} & \dfrac{im}{r}\hat{u} - \dfrac{1}{r}\hat{v} & \partial_z \hat{u} \\ \partial_r \hat{v} & \dfrac{im}{r}\hat{v} + \dfrac{1}{r}\hat{u} & \partial_z \hat{v} \\ \partial_r \hat{w} & \dfrac{im}{r}\hat{w} & \partial_z \hat{w} \end{pmatrix}. \tag{7}$$

The complex advection operator $\mathscr{C}_m$ in (6) is then defined as $\mathscr{C}_m(\hat{\boldsymbol{u}}^1, \boldsymbol{u^0}) = \boldsymbol{\nabla}_m\hat{\boldsymbol{u}}^1 \cdot \boldsymbol{u^0} + \boldsymbol{\nabla_0}\boldsymbol{u^0} \cdot \hat{\boldsymbol{u}}^1$ and accounts for the specific azimuthal periodicity of the normal mode. In the following, we restrict to the case of $|m| = 1$ disturbances. The associated global modes satisfy the following boundary conditions:

$$\partial_r\hat{u}^1 = \partial_r\hat{v}^1 = \hat{w}^1 = \hat{p}^1 = 0 \quad \text{on } \partial\Omega_{\mathrm{ax}} \text{ (axis)}, \tag{8a}$$

$$\hat{\boldsymbol{u}}^1 = \boldsymbol{0} \quad \text{on } \partial\Omega_{\mathrm{in}} \cup \partial\Omega_{\mathrm{bod}} \text{ (inlet and body)}, \tag{8b}$$

$$-\hat{p}^1\boldsymbol{n} + \mathrm{Re}^{-1}\boldsymbol{\nabla}_1\hat{\boldsymbol{u}}^1 \cdot \boldsymbol{n} = \boldsymbol{0} \text{ (no-stress)} \quad \text{on } \partial\Omega_{\mathrm{out}} \text{ (outlet)}, \tag{8c}$$

$$\hat{u}^1 = \partial_r\hat{v}^1 = \partial_r\hat{w}^1 = 0 \text{ (free slip)} \quad \text{on } \partial\Omega_{\mathrm{ext}} \text{ (external boundary)}, \tag{8d}$$

the condition at the axis $\partial\Omega_{\mathrm{ax}}$ being specific to the azimuthal wavenumbers $|m| = 1$. In the following, all quantities of interest will be presented using the representation used in Fig. 1, which corresponds to the azimuthal plane $\theta = 0$. For a given quantity whose normal mode expansion has been carried out, the knowledge of this particular distribution and of the azimuthal wavenumber m thus allows to deduce the corresponding distribution in all other azimuthal planes by rotation.

2.3. Adjoint global modes

The adjoint evolution operator $\mathscr{A}_m^\dagger$ is defined so that for any vectors $\hat{\boldsymbol{q}}^1$ fulfilling boundary conditions (8) and $\hat{\boldsymbol{q}}^{1\dagger}$ fulfilling boundary conditions to be determined,

$$\langle \hat{\boldsymbol{q}}^{1\dagger}, \mathscr{A}_m\hat{\boldsymbol{q}}^1 \rangle = \langle \mathscr{A}_m^\dagger\hat{\boldsymbol{q}}^{1\dagger}, \hat{\boldsymbol{q}}^1 \rangle, \tag{9}$$

with $\langle , \rangle$ being the inner product on Ω defined by $\langle \hat{\boldsymbol{a}}, \hat{\boldsymbol{b}} \rangle = \int_\Omega \hat{\boldsymbol{a}}^* \cdot \hat{\boldsymbol{b}}\, r\, \mathrm{d}r\, \mathrm{d}z$, where $\hat{\boldsymbol{a}}$ and $\hat{\boldsymbol{b}}$ belong to $\mathbb{C}^n$, the superscripted asterisk stands for the complex conjugate, and the dot refers to the canonic hermitian scalar product in $\mathbb{C}^n$. The adjoint equations are obtained using integration by parts of Eqs. (3) (Schmid and Henningson, 2002). The boundary conditions to be fulfilled by adjoint perturbations are such that all boundary terms arising during the integration are zero. For $|m| = 1$ disturbances, we obtain

$$\partial_r\hat{u}^{1\dagger} = \partial_r\hat{v}^{1\dagger} = \hat{w}^{1\dagger} = \hat{p}^{1\dagger} = 0 \quad \text{on } \partial\Omega_{\mathrm{ax}}, \tag{10a}$$

$$\hat{\boldsymbol{u}}^{1\dagger} = \boldsymbol{0} \quad \text{on } \partial\Omega_{\mathrm{in}} \cup \partial\Omega_{\mathrm{bod}}, \tag{10b}$$

$$(\boldsymbol{u^0} \cdot \boldsymbol{n})\hat{\boldsymbol{u}}^{1\dagger} + \hat{p}^{1\dagger}\boldsymbol{n} + \mathrm{Re}^{-1}\boldsymbol{\nabla}_1\hat{\boldsymbol{u}}^{1\dagger} \cdot \boldsymbol{n} = \boldsymbol{0} \quad \text{on } \partial\Omega_{\mathrm{out}}, \tag{10c}$$

$$\hat{u}^{1\dagger} = \partial_r\hat{v}^{1\dagger} = \partial_r\hat{w}^{1\dagger} = 0 \quad \text{on } \partial\Omega_{\mathrm{ext}}. \tag{10d}$$

With our notation, $\hat{\boldsymbol{q}}^{1\dagger}$ is then the solution of an eigenvalue problem that reads

$$(\sigma - i\omega)\mathscr{B}\hat{\boldsymbol{q}}^{1\dagger} + \mathscr{A}_m^\dagger\hat{\boldsymbol{q}}^{1\dagger} = \boldsymbol{0}, \tag{11}$$

where $\mathscr{A}_m^\dagger$ is the complex evolution operator defined as

$$\mathscr{A}_m^\dagger = \begin{pmatrix} \mathscr{C}_m^\dagger(\cdot, \boldsymbol{u}^0) - \dfrac{1}{\mathrm{Re}} \boldsymbol{\nabla}_m^2 & -\boldsymbol{\nabla}_m \\ \boldsymbol{\nabla}_m^{\mathrm{T}} & 0 \end{pmatrix}, \tag{12}$$

and $\mathscr{C}_m^\dagger(\hat{\boldsymbol{u}}^{1\dagger}, \boldsymbol{u}^0) = \boldsymbol{\nabla}_0 \boldsymbol{u}^{0\mathrm{T}} \cdot \hat{\boldsymbol{u}}^{1\dagger} - \boldsymbol{\nabla}_m \hat{\boldsymbol{u}}^{1\dagger} \cdot \boldsymbol{u}^0$ is the adjoint advection operator. Comparing $\mathscr{A}_m$ and $\mathscr{A}_m^\dagger$, we note that the non-normality comes only from the advection operator and can be split into two complementary effects. The *lift-up* type non-normality is due to the advection of the base flow by the perturbation, given by $\boldsymbol{\nabla}_0 \boldsymbol{u}^0 \cdot \hat{\boldsymbol{u}}^1$ for the direct operator $\mathscr{A}_m$ and $\boldsymbol{\nabla}_0 \boldsymbol{u}^{0\mathrm{T}} \cdot \hat{\boldsymbol{u}}^{1\dagger}$ for the adjoint operator $\mathscr{A}_m^\dagger$. When the flow is a simple parallel shear, this term gives rise to the so-called lift-up effect, linked to the generation of strong streamwise velocity perturbations by small displacements along the direction of the base flow gradient. The lift-up non-normality is then associated to direct and adjoint global modes that tend to be orthogonal one to the other because concentrated on different components of the velocity vector (Marquet et al., 2009). The convective non-normality (Chomaz et al., 1990; Chomaz, 2005; Marquet et al., 2009) is due to the transport of disturbances by the base flow, given by $\boldsymbol{\nabla}_m \hat{\boldsymbol{u}}^1 \cdot \boldsymbol{u}^0$ for the direct operator $\mathscr{A}_m$ and $-\boldsymbol{\nabla}_m \hat{\boldsymbol{u}}^{1\dagger} \cdot \boldsymbol{u}^0$ for the adjoint operator $\mathscr{A}_m^\dagger$, which have opposite signs. Physically, this indicates that direct perturbations are convected downstream and that adjoint perturbations are convected upstream (Chomaz, 2005). As noticed in Chomaz et al. (1990) in the case of the Ginzburg–Landau model equation, this non-normality is specific to open flows and tends to spatially separate the perturbation velocity fields, downstream for the direct perturbations and upstream for the adjoint perturbations. The convective non-normality is then associated to direct and adjoint global modes that tend to be orthogonal one to the other because localized in different regions of the flow. Of course, for real non-parallel flows, such as those considered here, both mechanisms act and the spatial structures of the direct and adjoint global modes result from their interactions (see Section 3).

As discussed in Chomaz (2005), the adjoint global mode may receive different physical interpretations. For an unstable flow, it defines the *most dangerous* initial perturbation of unit norm, i.e. that maximizes the large-time amplitude of the direct global mode (Schmid and Henningson, 2002; Chomaz, 2005). Presently, we will discuss only the physics of the initial perturbation but not its time evolution, that may lead to possibly energetic transient regimes before the large-time dynamics is reached.

For a marginally stable global mode, of growth rate $\sigma < 0$ ($|\sigma| \ll 1$) and of frequency ω, the adjoint global mode also characterizes the receptivity of the global mode to near-resonance harmonic forcing. This point is crucial in the perspective of active control, where the idea is to produce a large effect in the flow by introducing a small amount of energy, either by periodic blowing and suction at the wall or by use of a volumic force. If forcing occurs through a body force $\hat{\boldsymbol{f}} = (\hat{f}_r, \hat{f}_\theta, \hat{f}_z)^{\mathrm{T}}$ of frequency ω_f close to ω and of same azimuthal wavenumber as the global mode, the receptivity of the global mode, i.e. the amplitude of the forced global mode, is given by

$$\alpha = \frac{1}{\sigma + \mathrm{i}(\omega - \omega_f)} \frac{\langle \hat{\boldsymbol{q}}^{1\dagger}, (\hat{\boldsymbol{f}}, 0)^{\mathrm{T}} \rangle}{\langle \hat{\boldsymbol{q}}^{1\dagger}, \mathscr{B}\hat{\boldsymbol{q}}^1 \rangle}. \tag{13}$$

In the case of boundary forcing, for instance by periodic blowing and suction at the body wall $\partial\Omega_{\mathrm{bod}}$, also with the frequency ω and the same azimuthal wavenumber than that of the global mode, Giannetti and Luchini (2007) have computed the global mode amplitude as a function of the velocity $\hat{\boldsymbol{u}}_w$ imposed at the wall by modifying Eq. (8b) on $\partial\Omega_{\mathrm{bod}}$ into $\hat{\boldsymbol{u}}^1 = \hat{\boldsymbol{u}}_w$:

$$\alpha = \frac{1}{\mathrm{i}(\omega - \omega_f)} \frac{1}{\langle \hat{\boldsymbol{q}}^{1\dagger}, \mathscr{B}\hat{\boldsymbol{q}}^1 \rangle} \int_{\partial\Omega_{\mathrm{bod}}} \left(\hat{p}^{1\dagger} \boldsymbol{n} + \frac{1}{\mathrm{Re}} \boldsymbol{\nabla}_m \hat{\boldsymbol{u}}^{1\dagger} \cdot \boldsymbol{n} \right) \cdot \hat{\boldsymbol{u}}_w \, \mathrm{d}l. \tag{14}$$

The term arising from the Reynolds stresses is the only term sensitive to wall velocities that are tangential to the wall. It has been argued in previous studies that for sufficiently large Reynolds numbers (Marquet et al., 2009), this term can be neglected compared to the wall pressure $\hat{p}^{1\dagger}$, implying that the flow is receptive only to the wall-normal component of the velocity, and that the forcing is efficient only in regions of the wall where the magnitude of the adjoint wall pressure $|\hat{p}^{1\dagger}|$ is large. However, for transitional Reynolds numbers, the Reynolds stress contribution to the receptivity cannot be neglected. Indeed, it will be shown that this viscous contribution does remain negligible for wall-normal velocities but is significant for tangential forcing. Note that relations (13) and (14) are valid only for near-resonance forcing, when $\omega - \omega_f$ is small. They can be generalized to the case of off-resonance forcing by solving for the norm of the resolvent operator $(\omega_f \mathscr{B} + \mathrm{i}\mathscr{A}_m)^{-1}$ when a body force is added to the momentum equations (Schmid and Henningson, 2001).

The adjoint analysis is also useful to identify the region of the flow which acts as the 'wavemaker'. By considering small modifications of the evolution operator $\mathscr{A}_m$ with the form of a 'force–velocity' coupling, Giannetti and Luchini (2007) have argued that the sensitivity of the eigenvalue to such a local feedback is maximum in the region where the

product of the modulus of the direct and adjoint global modes is not zero, and that this overlapping region therefore identifies the wavemaker. This concept of sensitivity has been extended recently to assess how imposed steady base flow modifications or addition of a steady volumic force may alter the stability properties of flows, leading to the definition of the so-called sensitivity to base flow modifications or sensitivity to a steady force, respectively (Marquet et al., 2008). In the present paper, as in the study of Giannetti and Luchini (2007), we present only results pertaining to the sensitivity to a 'force–velocity' coupling that represents a straightforward identification of the wavemaker region, and can be also viewed as a feedback induced by an actuator located at the same station as the sensor.

3. Results

The FreeFem + + software (http://www.freefem.org) is used to generate the triangulation with the Delaunay–Voronoi algorithm. The mesh refinement is controlled by the vertex densities on both external and internal boundaries. A schematic of the mesh structure is depicted in Fig. 1 in the case of the sphere, the mesh structure being similar in the case of the disk, except that for computational reasons, the width of the disk L cannot be chosen strictly equal to zero, so that we have used the smallest possible value, corresponding to an aspect ratio $L/D = 10^{-3}$. To avoid any computational difficulty, a zone of width 0.05 and high vertex density (250 vertex per unit length) is defined at the axis $r = 0$ and around the body, corresponding to the shaded area shown in Fig. 1. The base flow equations, as well as the direct (5) and adjoint (11) generalized eigenvalue problems are numerically solved by a finite-element method, using the same mesh. The unknown velocity and pressure fields are spatially discretized using a basis of Taylor–Hood elements, i.e. P2 elements for velocities and P1 elements for pressure. All equations are first multiplied by r to avoid the singularity on the $r = 0$ axis. The associated variational formulation is then derived and spatially discretized on the mesh composed of triangular elements. The sparse matrices resulting from the projection of the variational formulations onto the basis of finite elements are built with the FreeFem + + software. The matrix inverses are then computed using the UMFPACK library, which consists in a sparse direct LU solver (Davis and Duff, 1997; Davis, 2004).

3.1. Base flow

For all the Reynolds numbers Re considered in this study, the base flow is stable to axisymmetric stationary perturbations, and time-marching a direct numerical simulation of Eqs. (1), with imposed axisymmetry and required boundary conditions provide us with an approximate guess solution of the steady base flow q^0. The steady base flow q^0 solution of the nonlinear equations (2) is then obtained using an iterative Newton method involving the resolution of simple linear problems. Details of the numerical method may be found in Barkley et al. (2002) and Sipp and Lebedev (2007). In the present study, the iterative process is carried out until the $\mathscr{L}^2$-norm of the residual of the governing equations for q^0 becomes smaller than 10^{-12}. Fig. 2(a) shows isocontours of the base flow streamwise velocity w^0 computed for the disk at Re = 116.9. Note that since the base flow is axisymmetric, the spatial distribution of w^0 is identical in all other azimuthal planes. The solid line is the streamline linking the separation point to the stagnation point on the $r = 0$ axis; it defines the separatrix delimiting the recirculation bubble behind the disk. The negative values of the streamwise velocity close to the axis reaches 60% of the free-stream velocity, whereas in the case of the sphere, shown in Fig. 2(b) for Re = 212.6, this value does not exceed 40%. In the case of the disk, the pressure component of the base flow is expected to be singular at the edge of the disk, as predicted by Moffatt (1964). In the present numerical study, the thickness of the disk is small but finite, and the pressure singularity is smoothed out at the very scale of the
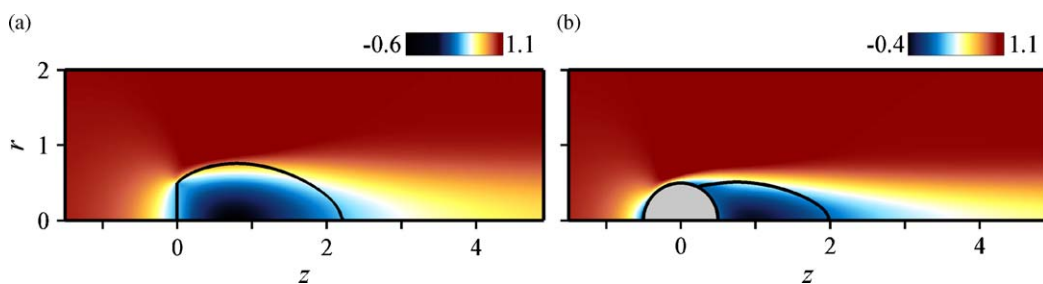

Fig. 2. Base flow at the threshold of the first instability. Isocontours of streamwise velocity w^0. The solid line indicates the separated bubble. (a) Disk at $\mathrm{Re}_A = 116.9$. (b) Sphere at $\mathrm{Re}_A = 212.6$.

disk. In order to assess the accuracy of the numerical method, the drag coefficient C_d and recirculation length L were computed for the sphere wake. The values obtained at Re = 100 ($L = 1.369$, $C_d = 1.087$) and Re = 200 ($L = 1.934$, $C_d = 0.770$) show excellent agreement with the calculations obtained by Fornberg (1988) using finite-difference methods ($L = 1.373$, $C_d = 1.085$ at Re = 100 and $L = 1.934$, $C_d = 0.768$ at Re = 200, respectively).

3.2. Stability analysis

To compute the leading eigenvalues of operators $\mathscr{A}_1$ and $\mathscr{A}_1^\dagger$, which are responsible for the successive instabilities, we use a shift and invert strategy (Ehrenstein and Gallaire, 2005). The generalized eigenvalue problems are solved using the 'implicitly restarted Arnoldi method' of the ARPACK library.

Since the adjoint problem (11) has been formulated for continuous operators with associated adjoint boundary conditions, the spatial discretization of operators $\mathscr{A}_1$ and $\mathscr{A}_1^\dagger$ leads to discrete operators that are not hermitian one to the other because the operator $\mathscr{B}$ involved in the right-hand side of problems (5) and (11) does not correspond to the scalar product in cylindrical coordinates. We check *a posteriori* that the adjoint eigenvalues are complex conjugate with the direct eigenvalues and that a bi-orthogonality relation (Chomaz, 2005) is satisfied for the 10 leading global modes (i.e. that the scalar product of one of the 10 leading adjoint modes with any of the 10 leading direct global modes associated to a different eigenvalue is less that 10^{-7}), and conclude that our numerical procedure accurately estimates the direct and adjoint global modes.

Direct global modes are normalized by imposing the phase of the radial velocity to be zero at a particular location, i.e. $\hat{u}^1(0,1)$ must be real positive. The eigenmode energy is then normalized to unity in a fixed domain Ω_{in} defined arbitrarily as $z \in [-2.5, 5.25]$ and $r < 2$ and corresponding to the inner box in Fig. 1: $\langle \hat{\boldsymbol{q}}^1, \delta_{\text{in}} \mathscr{B} \hat{\boldsymbol{q}}^1 \rangle = 1$, with δ_{in} the function defined by $\delta_{\text{in}}(r,z) = 1$ if $(r,z) \in \Omega_{\text{in}}$ and 0 otherwise. The adjoint global modes are then normalized so that $\langle \hat{\boldsymbol{q}}^{1\dagger}, \mathscr{B} \hat{\boldsymbol{q}}^1 \rangle = 1$. Note that owing to the symmetries of the problem, Eqs. (5) and (12) remain invariant under the transformation $(\hat{u}^1, \hat{v}^1, \hat{w}^1, \hat{p}^1, m) \to (\hat{u}^1, -\hat{v}^1, \hat{w}^1, \hat{p}^1, -m)$, so that we need to investigated only the case $m = 1$.

3.3. Stationary global mode

When the Reynolds number is increased from small values, a first stationary mode ($\omega = 0$) destabilizes the axisymmetric base flow at Re_A, both for the disk and the sphere. In the following, this mode is named mode A and the corresponding eigenvector is referred to as $\hat{\boldsymbol{q}}_A^1$. The critical Reynolds number Z is $\text{Re}_A = 116.9$ for the disk and $\text{Re}_A = 212.6$ for the sphere. Fig. 3(a) shows the spatial structure of the streamwise velocity component $\hat{w}_A^1$ for the disk. Since the azimuthal wavenumber is $m = 1$, the associated spatial distribution of w_A^1 for an angle θ is obtained as $w_A^1(r, \theta, z) = \hat{w}_A^1(r, z) e^{i\theta}$. In particular for $\theta = \pi$, we have simply $w_A^1(r, \pi, z) = -\hat{w}_A^1(r, z)$. The global mode is dominated by axially extended streamwise velocity disturbances located downstream of the disk, that induce an off-axis displacement of the wake (Johnson and Patel, 1999; Thompson et al., 2001). The associated adjoint global mode $\hat{\boldsymbol{q}}_A^{1\dagger}$ is presented in Fig. 3(b). The adjoint global mode presents high magnitudes of adjoint streamwise velocity $\hat{w}_A^{1\dagger}$ within the recirculating bubble and close to the body, and low magnitude disturbances upstream of thedisk. The downstream and upstream localizations of the direct and adjoint global modes resulting from the convective non-normality of the linearized Navier–Stokes operator are further evidenced in Figs. 3(c) and (d). Fig. 3(c) shows the streamwise evolution of the amplitude of the direct global mode, computed as the density energy integrated over a vertical cross-section for each streamwise position, i.e. $E_A(z) = \int_0^{r_\infty} |\hat{\boldsymbol{u}}_A^1(r,z)|^2 r \, \mathrm{d}r$, as well as the contribution of the streamwise velocity to this amplitude $E_A(z)$, i.e. $S_A(z) = \int_0^{r_\infty} |\hat{w}_A^1(r,z)|^2 r \, \mathrm{d}r$. The direct mode is nil upstream of the body, reaches a maximum in the recirculating bubble, and decreases slowly downstream of the body. The contribution of the streamwise velocity to the direct global mode dominates the entire field. Fig. 3(d) shows similarly the streamwise distribution of energy density for the adjoint global mode, i.e. $E_A^\dagger(z) = \int_0^{r_\infty} |\hat{w}_A^{1\dagger}(r,z)|^2 r \, \mathrm{d}r$, as well as the contribution of the cross-stream velocity components to this amplitude $E_A^\dagger(z)$, i.e. $C_A^\dagger(z) = \int_0^{r_\infty} (|\hat{u}_A^{1\dagger}|^2 + |\hat{v}_A^{1\dagger}|^2) r \, \mathrm{d}r$. The adjoint global mode vanishes downstream of the body, and reaches a maximum in the recirculating area. Upstream of the body, its energy density is two orders of magnitude smaller than in the recirculation bubble and decreases exponentially. In regions of the flow where the amplitude of the adjoint global mode is larger than 10^{-1}, in particular in the whole recirculating bubble, the contribution of the cross-stream velocity components to the adjoint global mode dominates the adjoint field. For this first unstable mode A, the direct and adjoint global modes are concentrated on different components of the velocity vector, the streamwise and cross-stream velocity components, respectively, suggesting that the lift-up mechanism plays a significant role in the dynamics of the stationary mode. Furthermore, the direct and adjoint global modes are mainly
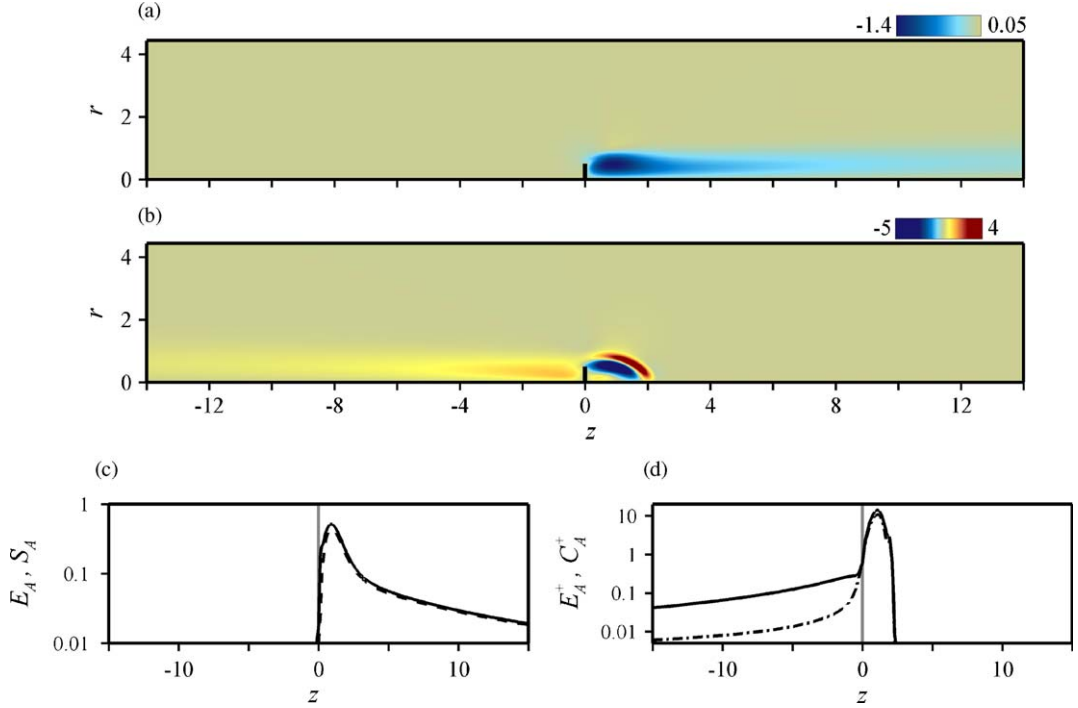
Fig. 3. Steady direct and adjoint global modes A for the disk at threshold, $\mathrm{Re}_A = 116.9$. (a) Spatial distribution of streamwise velocity $\hat{w}_A^1$. (b) Spatial distribution of adjoint streamwise velocity $\hat{w}_A^{1\dagger}$. (c) Streamwise distribution of energy density $E_A(z)$ for the direct global mode. The dashed line shows the contribution $S_A(z)$ of the streamwise velocity component to the energy $E_A(z)$. The vertical grey line marks the position of the separation point. (d) Streamwise distribution of energy density $E_A^\dagger(z)$ for the adjoint global mode. The dash-dotted line shows the contribution of the adjoint cross-stream velocity components $C_A^\dagger(z)$ to the energy $E_A^\dagger(z)$. The vertical grey line marks the position of the separation point.

localized in the recirculation, with, respectively, downstream and upstream tails showing the influence of the convective non-normality which, for the present flow, is moderate since the amplitude are small away from the recirculation bubble. The non-normality may be quantified by the angle θ_A defined as

$$\cos\left(\frac{\pi}{2} - \theta_A\right) = \frac{\langle \hat{q}_A^{1\dagger}, \mathscr{B}\hat{q}_A^1 \rangle}{\langle \hat{q}_A^{1\dagger}, \mathscr{B}\hat{q}_A^{1\dagger} \rangle^{1/2} \times \langle \hat{q}_A^1, \mathscr{B}\hat{q}_A^1 \rangle^{1/2}}, \tag{15}$$

with $\langle \hat{q}_A^{1\dagger}, \mathscr{B}\hat{q}_A^1 \rangle = 1$ by convention here. The non-normality is thus measured by the departure θ_A to $\pi/2$ of the angle between the direct and adjoint global modes, i.e. the larger the non-normality, the smaller θ_A. Note that it is also possible to measure the non-normality of the global mode as the inverse of the scalar product of the normalized direct and adjoint eigenmodes. In this case, a large non-normality is associated to small values of the scalar product. It is worthwhile noting that both measures are closely connected, since the latter measure then simply corresponds to the inverse of $\sin\theta_A$.

We define the streamwise amplitude of a complex velocity field $\hat{u}(r, z)$ as the norm $\|\hat{u}\|_L^2(z) = \int_0^{r_\infty} |\hat{u}|^2 r\, dr$. We propose to quantify the contribution of the convective non-normality to the overall non-normality by considering the parameter γ defined by

$$\gamma = 1 - \frac{\int_{z_{-\infty}}^{z_\infty} \|\hat{u}^1\|_L \times \|\hat{u}^{1\dagger}\|_L\, dz}{(\int_{z_{-\infty}}^{z_\infty} \|\hat{u}^1\|_L^2\, dz)^{1/2} \times (\int_{z_{-\infty}}^{z_\infty} \|\hat{u}^{1\dagger}\|_L^2\, dz)^{1/2}} = 1 - \frac{\int_{z_{-\infty}}^{z_\infty} \|\hat{u}^1\|_L \times \|\hat{u}^{1\dagger}\|_L\, dz}{\langle \hat{q}_A^{1\dagger}, \mathscr{B}\hat{q}_A^{1\dagger} \rangle^{1/2} \times \langle \hat{q}_A^1, \mathscr{B}\hat{q}_A^1 \rangle^{1/2}}. \tag{16}$$

Using a standard Cauchy–Schwartz inequality, it can be shown that $0 \leqslant \gamma \leqslant 1$. A value of γ close to 0 is reached if $\|\hat{u}_A^1\|_L = \beta \|\hat{u}_A^{1\dagger}\|_L$, meaning that the direct and adjoint global modes have the same spatial distribution of energy. In that case, the convective non-normality is not active since it would imply a dissymmetry in the distribution of the direct and adjoint modes. On the contrary, a value of γ close to 1 means that the direct and adjoint global modes are spatially separated. For the disk, we find presently that $\theta_A = 0.17$ (10°) and $\gamma_A = 0.40$, meaning that the non-normality of mode
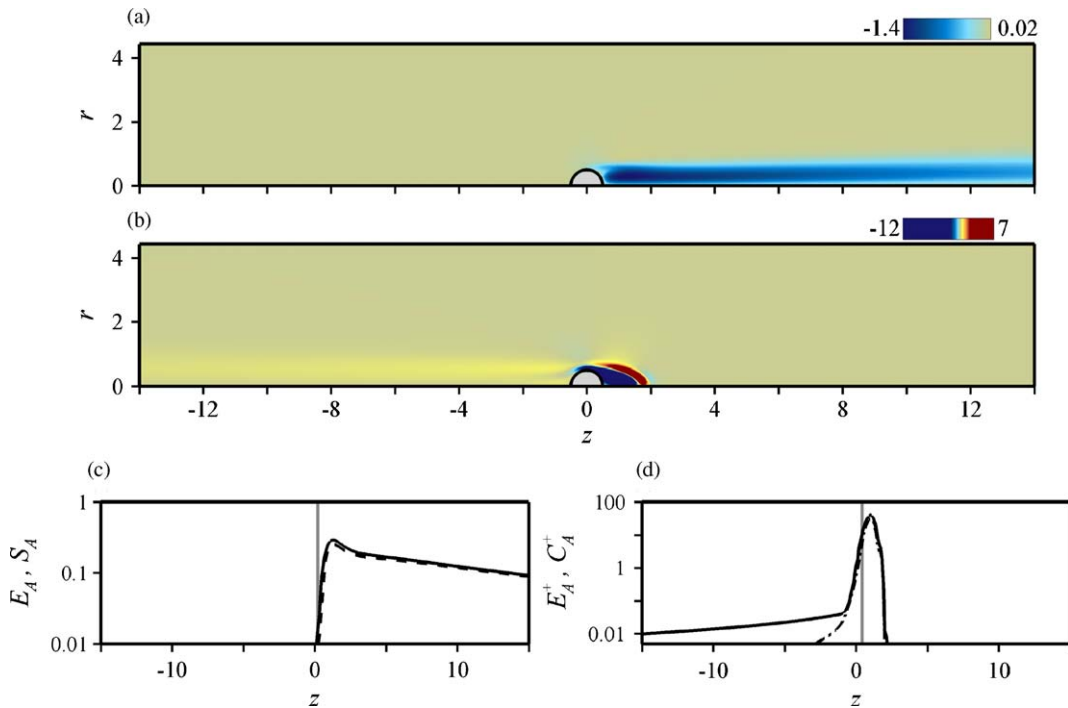
Fig. 4. Same as Fig. 3 for the stationary direct and adjoint global modes A of the sphere, $\mathrm{Re}_A = 212.6$.

A is moderate and due to the convective non-normality at most at 40%, which confirms the importance of the lift-up mechanism.

Fig. 4 shows the marginally stable stationary mode A and its adjoint global mode for the sphere. The general dynamics is identical to that described in Fig. 3 in the case of the disk, indicating that the instability results from similar physical mechanisms in both flows. The direct mode is led by the streamwise velocity component downstream of the sphere and the adjoint global mode is even more concentrated in the recirculation bubble, reaching a maximum just downstream of the separation point marked by the vertical grey line in Figs. 4(c) and (d). The cross-stream velocity components dominate in the recirculating area. In the case of the sphere, the energy density of the direct global mode decays downstream slower than in the case of the disk and the adjoint mode presents a weaker upstream energy density. At the separation point, the adjoint global mode exhibits an energy density larger by one order of magnitude than that found for the disk. The non-normality of the sphere, as quantified by $\theta_A = 0.07$ ($4°$), is significantly larger than that of the disk. The contribution of the convective non-normality evaluated by γ_A is 0.76, and is also more important than in the case of the disk. This shows that the wake of the sphere is more receptive to initial perturbation or forcing (both being $m = 1$ stationary), in particular close to the separation line.

The magnitude of the product between the modulus of the direct and adjoint global modes is shown for the disk and the sphere in Figs. 5(a) and (b), where the white solid lines stand for the separation lines. For both bodies, the product is almost nil everywhere in the flow, except close to the body, along the separation line, and in the centre of the recirculation bubble where the largest values are reached. This specific spatial localization results from the convective non-normality that induces the downstream and upstream localizations of the direct and adjoint global modes. The similarity in the results for the disk and the sphere suggests the existence of a single wavemaker for this instability for both shapes of bodies, located in the core of the recirculation. Following the argument of Giannetti and Luchini (2007), passive control of the stationary $m = 1$ eigenmode should induce modifications of the base flow close to the core of the recirculation to achieve a maximum stabilizing or destabilizing effect. As already commented, the sensitivity quantified in Fig. 5 is rigorous for a local 'force–velocity' coupling (Giannetti and Luchini, 2007), i.e. the effect of a local body force actuation proportional to the signal of a velocity sensor located at the exact same station. By extrapolation, it describes the effect of a steady base flow modification but only qualitatively since the modified advection operator involves also the gradients of the perturbation velocity. Note that in the recirculating bubble, the sphere exhibits a 'force–velocity' sensitivity larger than that of the disk, suggesting that the wake of the sphere would be more controllable through the use of passive devices.
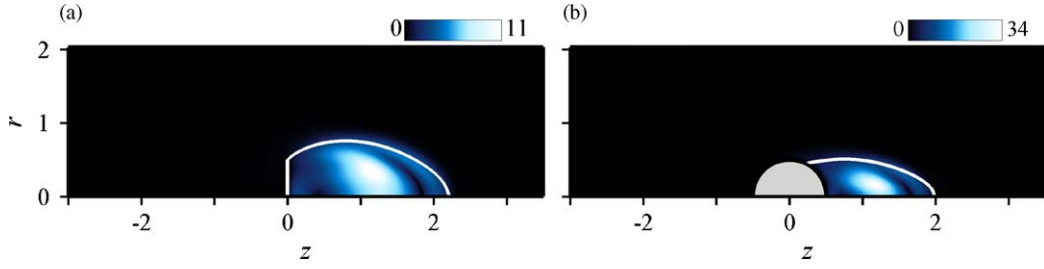
Fig. 5. Receptivity to local modifications of the linearized evolution operator corresponding to a local 'force–velocity' coupling (Giannetti and Luchini, 2007) for the stationary mode A, quantified by the field $|\hat{u}_A^{1\dagger}| \times |\hat{u}_A^1|(r,z)$. (a) Disk at $\mathrm{Re}_A = 116.9$. (b) Sphere at $\mathrm{Re}_A = 212.6$.

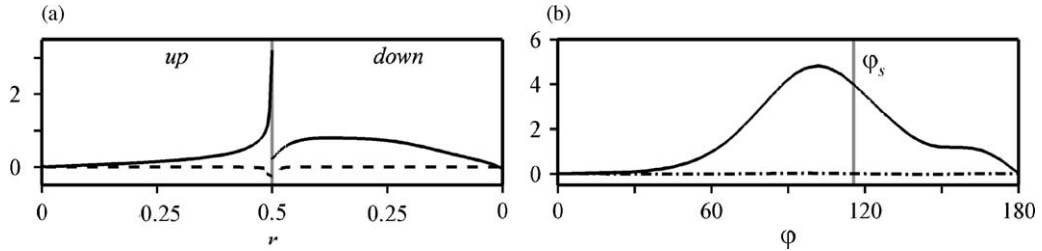Fig. 6. Receptivity of the global mode A to blowing and suction: (a) As a function of the radius for the disk at $\mathrm{Re}_A = 116.9$. (b) As a function of the angle from the leading stagnation point for the sphere at $\mathrm{Re}_A = 212.6$. The solid lines correspond to the adjoint pressure distribution $\hat{p}_A^{1\dagger}$ and the dashed lines to the normal component of the Reynolds stress contribution $\mathrm{Re}_A^{-1}(\nabla_1\hat{u}_A^{1\dagger} \cdot \boldsymbol{n}) \cdot \boldsymbol{n}$. The vertical grey line marks the position of the separation point.

The solid lines in Figs. 6(a) and (b) present the distributions of the magnitude of adjoint pressure $\hat{p}_A^{1\dagger}$ on the body walls, which, following relation (14), quantifies the receptivity to a stationary $m = 1$ blowing and suction. For the disk, results are presented as a function of the radial position r, on the upstream and downstream walls of the body. The upstream wall exhibits significantly larger receptivity to blowing and suction than the downstream wall. Moreover, the upstream adjoint pressure distribution increases significantly close to the separation point, where the maximum value is reached. The dashed lines present the normal component of the receptivity term arising from the Reynolds stress contribution in (14), i.e. $\mathrm{Re}_A^{-1}(\nabla_1\hat{u}_A^{1\dagger} \cdot \boldsymbol{n}) \cdot \boldsymbol{n}$. It can be seen that for both body shapes, the magnitude of this viscous correction remains negligible compared to the maximum magnitude of adjoint pressure, even at the moderately high Reynolds numbers under consideration. In the case of active control by blowing and suction, an actuator that imposes a stationary $m = 1$ normal wall velocity will achieve maximum efficiency if placed at the edge of the forward facing side of the disk. One may note that a small permanent tilt of the disk corresponds to a small $m = 1$ wall displacement that may be modelled as an equivalent blowing and suction of magnitude proportional to the distance to the axis, and may therefore force efficiently the stationary mode A.

For the sphere, results are presented as a function of the azimuthal position φ, the origin of φ being taken at the leading stagnation point $(-0.5, 0)$. The vertical grey line is located at the separation point, corresponding to $\varphi_s = 116°$. The adjoint pressure $\hat{p}_A^{1\dagger}$ is zero on the axis, owing to the boundary conditions. The magnitude of adjoint pressure reaches a maximum for $\varphi = 102°$, upstream from the separation point. The level then decreases slowly as one moves away from this optimal position, the magnitude of adjoint pressure remaining significant in the range $\varphi \in [80°, 130°]$. The adjoint pressure level decreases upstream and becomes zero at the leading stagnation point. The main difference with the disk is that the region where the $m = 1$ blowing and suction is efficient is extremely extended with large receptivity values everywhere, except close to the stagnation points. Therefore, for the sphere, the actuator would be slightly more efficient if placed just upstream from the separation (and not at the separation) but its precise location is less important. In contrast, controlling the disk wake will be efficient solely if the actuator is precisely positioned.

Normal-to-the-wall blowing and suction is not the only way to control the flow at the wall. Active control can also be achieved by imposing a tangential velocity, for which the relevant receptivity is given by the tangential components of the viscous stress tensor, i.e. $\mathrm{Re}_A^{-1}(\nabla_1\hat{u}_A^{1\dagger} \cdot \boldsymbol{n}) \cdot \boldsymbol{t}^i$, where $\boldsymbol{t}^i$ ($i = 1, 2$) are the tangential vectors oriented along the azimuthal and orthoradial directions. The maximum magnitude of this contribution represents less than 8% of the maximum adjoint pressure in the case of the disk but 25% in the case of the sphere. A convenient and efficient way of
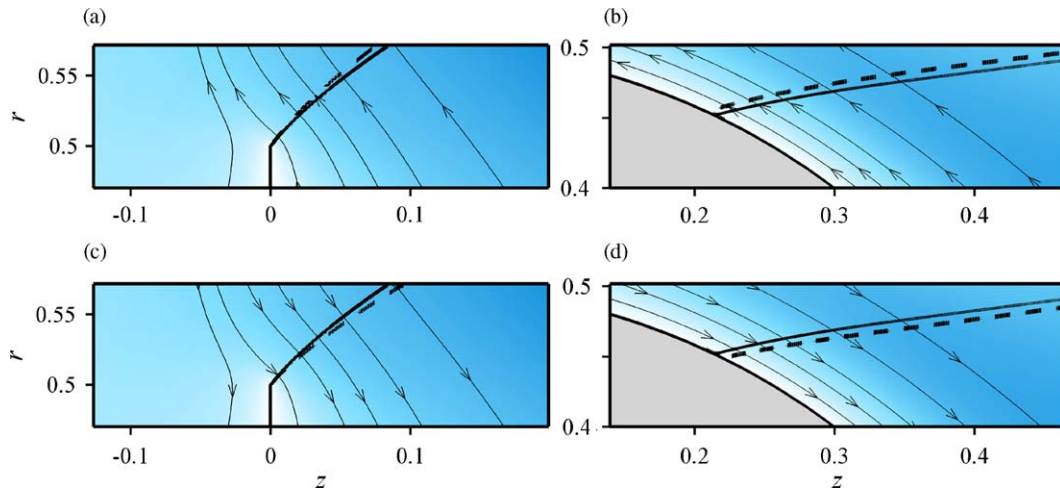
Fig. 7. Optimal initial perturbation for the stationary instability. The solid and dashed lines stand for the separation line of the base flow and of the total flow $q^0 + \varepsilon \hat{q}_A^{1\dagger}$, respectively. (a) Disk at $\mathrm{Re}_A = 116.9$: magnified view of the adjoint velocity field $\hat{u}_A^{1\dagger}$ close to the separation in the azimuthal plane $\theta = 0$. Blue and white regions correspond, respectively, to large and low values of the adjoint velocity magnitude, its orientation being shown by the streamlines. (b) Same as (a), but for the sphere at $\mathrm{Re}_A = 212.6$. (c) and (d) Same as (a) and (b), in the azimuthal plane $\theta = \pi$.

realizing such a control by tangential forcing would then be to rotate the sphere. However, this receptivity, predicted at the critical Reynolds number, should decrease as the Reynolds number increases.

As mentioned previously, the adjoint global mode also represents *the most dangerous* initial velocity perturbation, since for a fixed initial energy of the perturbation, it maximizes the large-time amplitude of the direct mode A. The effect of the optimal initial perturbation may be physically interpreted by considering the flow reconstructed as the linear superposition of the base flow q^0 and the adjoint global mode $\hat{q}_A^{1\dagger}$ with a finite amplitude ε. For the disk, ε is chosen equal to 2.4×10^{-2} so that the maximum streamwise velocity perturbation represents 10% of the maximum streamwise velocity $w_{\max}^0$. Figs. 7(a) and (c) show the streamlines of the adjoint global mode in the region of the separation point in the azimuthal planes $\theta = 0$ and π. The solid and dashed lines stand for the separation line of the base flow and of the total flow $q^0 + \varepsilon \hat{q}_A^{1\dagger}$, respectively. The levels of adjoint velocity amplitude are indicated by the colour shading, where dark regions stand for high perturbation velocities. Close to the separation point, the streamlines are normal to the separation line, and oriented upstream (resp. downstream) for $\theta = 0$ (resp. $\theta = \pi$). Consequently, the separation line is tilted upstream and downstream as we move along in the azimuthal direction, the extremity of the line remaining pinned at the disk rim. The optimal initial perturbation corresponds therefore to a stationary azimuthal modulation of the separation angle with respect to that of the base flow. In the case of the sphere, owing to the larger receptivity of the wake, ε is chosen much smaller ($\varepsilon = 9.3 \times 10^{-4}$) so that the maximum streamwise velocity perturbation represents 1% of the maximum streamwise velocity $w_{\max}^0$. Figs. 7(b) and (d) show that the streamlines of the optimal initial perturbation are parallel to the sphere surface, and induce a displacement with no tilt of the separation line, in agreement with the physical intuition that the separation line is no more pinned by the bluff geometry of the body. The separation point is hence displaced upstream and downstream, so that the optimal initial perturbation, given by the adjoint global mode, corresponds to a stationary displacement of the separation point in the streamwise direction which ondulates in the azimuthal direction.

3.4. Oscillating global mode

The second instability occurs at Re_B for an oscillating mode of frequency $\omega = \omega_0$. The associated mode is named mode B and the corresponding eigenvector is referred to as $\hat{q}_B^1$. The critical Reynolds numbers and frequency are $\mathrm{Re}_B = 125.3$, $\omega_0 = 0.760$ for the disk and $\mathrm{Re}_B = 280.7$, $\omega_0 = 0.699$ for the sphere, the corresponding Strouhal numbers $\mathrm{St} = \omega_0 D/(2\pi U_\infty)$ being 0.121 and 0.111, respectively. Figs. 8(a) and 9(a) show the spatial structure of the streamwise velocity $\hat{w}_B^1$ at the instability threshold for the disk and the sphere. Since the frequency is not zero, the eigenmode $\hat{q}_B^1$ is complex but we restrict the description to the real part $\hat{q}_{Br}^1$ of the eigenvector, as its imaginary part displays a similar
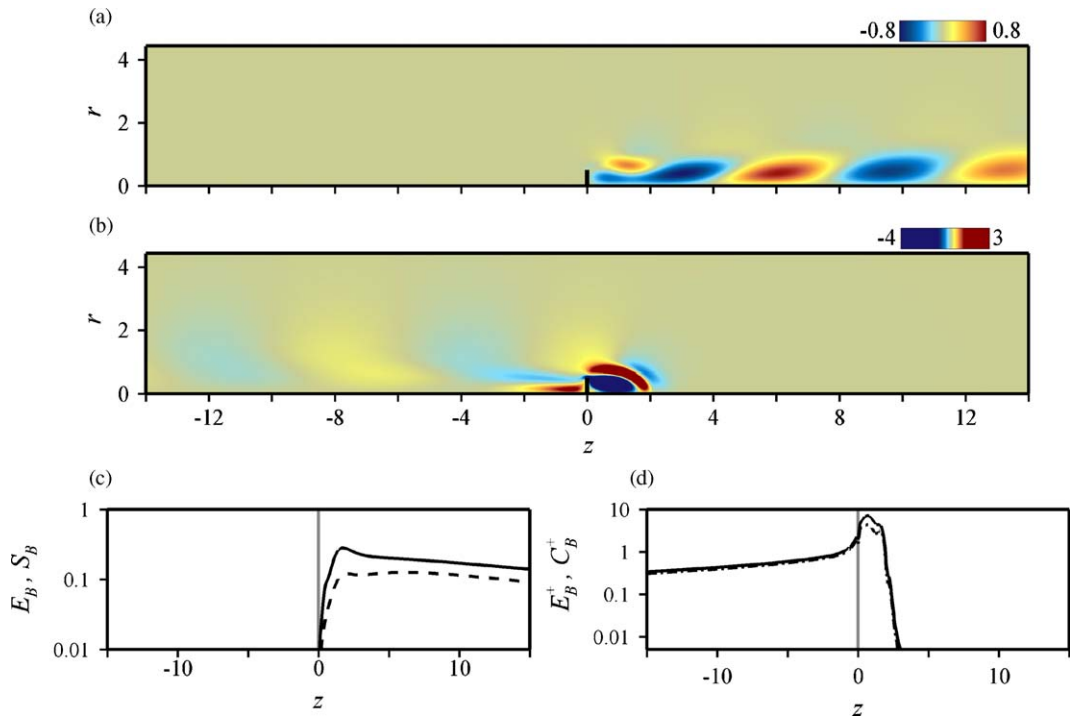
Fig. 8. Same as Fig. 3 for the oscillating instability of the disk, $Re_B = 125.3$.
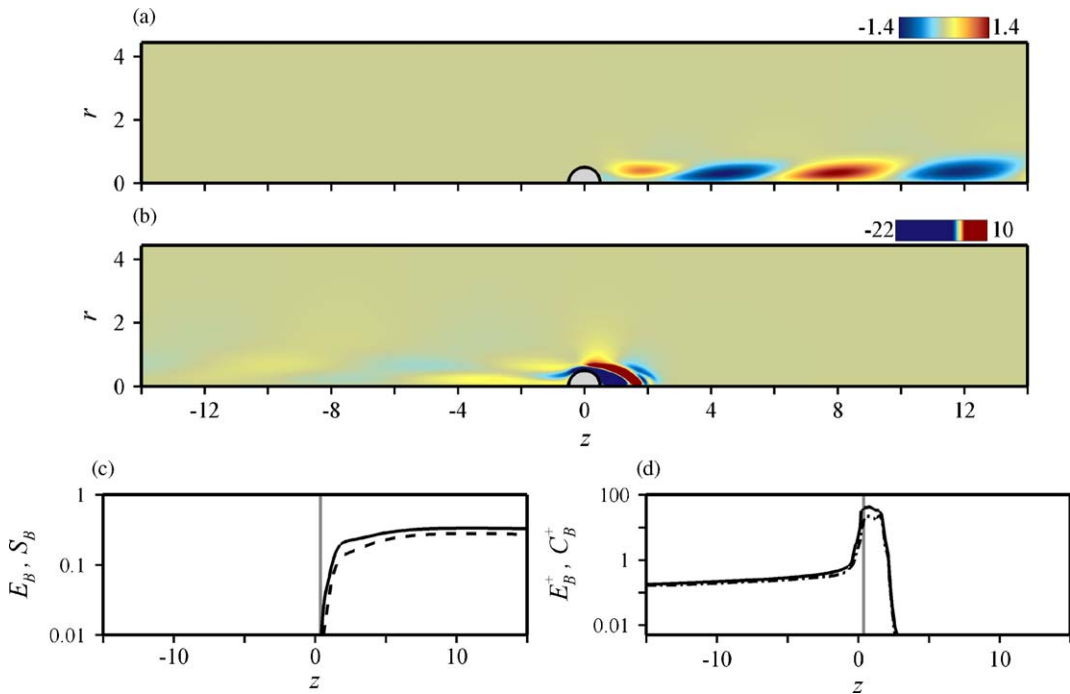

Fig. 9. Same as Fig. 3 for the oscillating instability of the sphere, $Re_B = 280.7$.

structure, but approximately in spatial quadrature, indicating that this global mode B corresponds to a spiralling perturbation behind the body, which rotates in time at the frequency ω_0. Note that, because of the symmetries of the problem, the mirror spiral mode rotating in time at the same frequency but in the opposite azimuthal direction also

destabilizes the base flow. The general dynamics is identical for the disk and the sphere, the direct modes B exhibiting periodic positive and negative velocity perturbations downstream of the body. The adjoint global modes B are shown in Figs. 8(b) and 9(b). Again, we discuss only the real part of the eigenvector $\hat{q}_{Br}^{1\dagger}$, as its imaginary part displays a similar structure in spatial quadrature. The localization of the adjoint global mode B is similar to that of the adjoint global mode A discussed above. For the disk and the sphere, the oscillating adjoint global modes B exhibit large streamwise velocities $\hat{w}_B^{1\dagger}$ within the recirculating area and close to the body. They also display velocity disturbances upstream of the disk and the sphere under the form of low magnitude periodic structures, visible despite their low amplitude by an appropriate choice of the colour look-up table in Figs. 8(b) and 9(b). Note that the absolute magnitude of these structures is slightly larger in the case of the sphere compared to the disk. The downstream and upstream localizations of the direct and adjoint global modes are further evidenced in Figs. 8(c) and (d) for the disk and in Figs. 9(c) and (d) for the sphere. Figs. 8(c) and 9(c) show the streamwise distribution of energy density $E_B(z)$ of the direct global modes (solid line), as well as the contribution of the streamwise velocity $S_B(z)$ to this energy (dashed line). We find that the direct mode is evanescent upstream of the body and reaches a maximum in the recirculating area. The downstream evolution differs between the disk, where the energy density decreases slowly, and the sphere, where the fluctuations keep increasing downstream. Figs. 8(d) and 9(d) show similarly the streamwise distribution of energy density $E_B^\dagger(z)$ of the adjoint global mode (solid line), as well as the contribution of the cross-stream velocity components $C_B^\dagger(z)$ to this energy (dash-dotted line). The adjoint global mode vanishes downstream of the body, reaches a maximum in the recirculating area and decreases steadily upstream of the body. In the vicinity of the separation point, the contribution of the cross-stream velocity components to the adjoint global mode dominates. For both geometries, the contribution of streamwise velocity no more dominates the entire direct field, so that the contribution of the lift-up mechanism to the structure of the direct global mode B is less important than for the stationary global mode A. It can be seen, by comparing Figs. 8(d) and 9(d), that in the case of the sphere, the oscillating adjoint global mode B exhibits an amplitude close to the separation point larger by almost one order of magnitude than that found for the disk. The overall non-normality is important as we find here that $\theta_B = 0.07$ (4°) for the disk and 0.02 (1°) for the sphere. This indicates that the oscillating global modes B are more receptive to initial perturbation or forcing than the stationary global modes A, the wake of the sphere being more receptive than that of the disk. We find for the convective non-normality parameter $\gamma_B = 0.88$ for the disk and 0.94 for the sphere. These values are significantly more important than in the case of the stationary global mode A, suggesting that the overall non-normality is almost entirely due to the convective non-normality resulting in the streamwise separation of the direct and adjoint global modes.

The magnitude of the product between the modulus of the direct and adjoint global modes is shown for the disk and the sphere in Figs. 10(a) and (b). The similarity between both flows suggests, for mode B also, the existence of a single physical mechanism for the oscillating instability, with the recirculating bubble acting as the wavemaker. The results are somehow reminiscent of that discussed for the first stationary instability of mode A, with a product almost nil everywhere in the flow, except within the recirculation zone. However, comparing to mode A, the largest values are reached along the separation line and no more in the core of the recirculation. This suggests that shear instability is the physical mechanism responsible for the development of spiral modes B. In the case of passive control, the base flow modifications should therefore be induced close to the separation line to achieve maximum efficiency. Note that in the recirculating area, the sphere exhibits an amplitude significantly larger than that of the disk, indicating that the wake of the sphere is more sensitive to local modifications of the evolution operator.

In the case of the control of the oscillating instability via wall-normal blowing and suction, the contribution of the Reynolds stress $Re_B^{-1}\nabla_1\hat{u}_B^{1\dagger} \cdot n$ is weak compared to the maximum level of adjoint pressure, a result similar to that evidenced for the stationary instability. Relation (14) thus indicates that only the magnitude of adjoint pressure $|\hat{p}_B^{1\dagger}|$ determines the receptivity of the global mode, whereas the individual real and imaginary parts $\hat{p}_{Br}^{1\dagger}$ and $\hat{p}_{Bi}^{1\dagger}$ are useful to predict the phase of the response of the forced global mode relative to that of the oscillating wall forcing. Figs. 11(a) and (b) present the distributions of the magnitude of adjoint pressure $|\hat{p}_B^{1\dagger}|$ on the body walls. The distributions are amazingly similar to that found for the stationary instability. For the disk, the magnitude is larger on the upstream wall where the adjoint pressure distribution increases significantly at the edge. For the sphere, the magnitude of adjoint pressure is maximum for $\varphi = 86°$, upstream from the separation point located at $\varphi_s = 112°$. It decreases slowly as one moves away from this optimal position, the magnitude of adjoint pressure remaining significant in the range $\varphi \in [75°, 115°]$. Therefore, in the case of active control, an actuator that imposes a periodic $m = 1$ blowing or suction at the frequency ω_0 should be placed at the rime on the forward facing side of the disk, and upstream from the separation in the case of the sphere to be most efficient. Similarly to the results obtained for the stationary instability of mode A, one may achieve good efficiency by moving the actuator position around the separation point of the sphere, as the region of receptivity is quite large. The main difference between both instabilities is that the magnitude of adjoint pressure levels are higher for the oscillating instability of mode B. Therefore, one may expect that the control of the oscillating instability will be less expensive than that of the stationary instability, i.e. that one will obtain the same
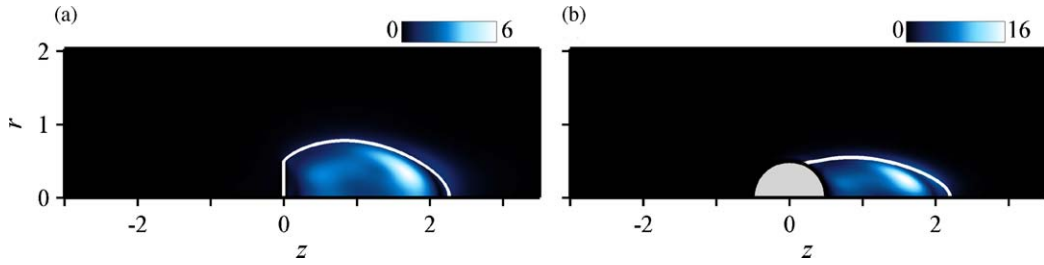
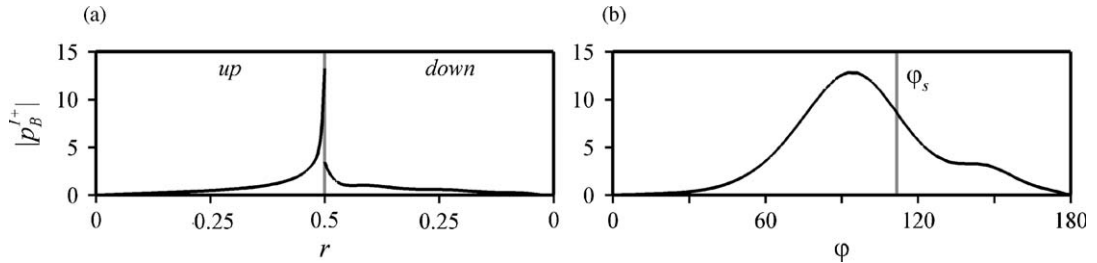Fig. 10. Same as Fig. 5 for the oscillating mode B. (a) Disk at $\mathrm{Re}_B = 125.3$. (b) Sphere at $\mathrm{Re}_B = 280.7$.

Fig. 11. Same as Fig. 6 for the adjoint pressure distribution of the oscillating mode B. (a) Disk at $\mathrm{Re}_B = 125.3$. (b) Sphere at $\mathrm{Re}_B = 280.7$.
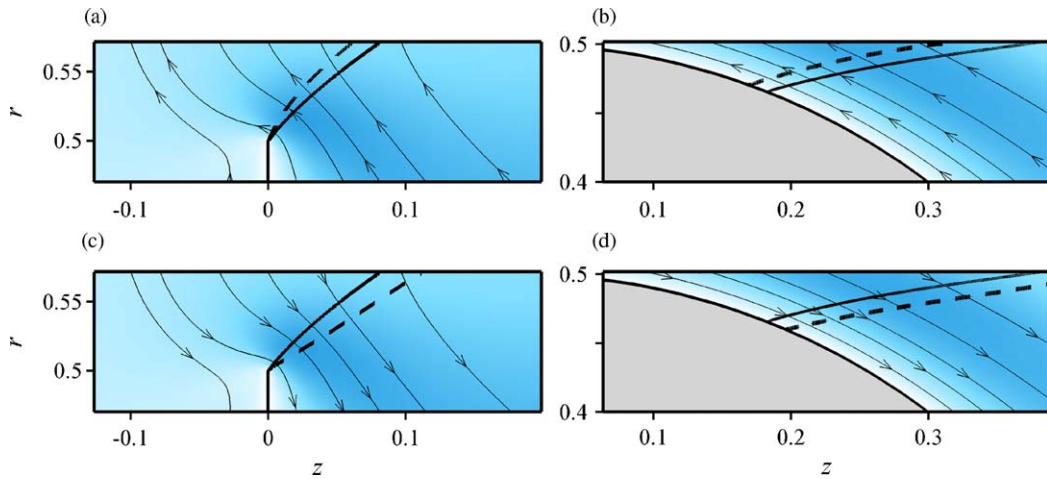

Fig. 12. Same as Fig. 7 for the oscillating mode B. (a)–(c) Disk at $\mathrm{Re}_B = 125.3$. (b)–(d) Sphere at $\mathrm{Re}_B = 280.7$.

amplitude of forced global mode by introducing less energy in the flow. In the case of tangential forcing, the maximum magnitude of this contribution represents less than 5% of the maximum adjoint pressure in the case of the disk but 25% in the case of the sphere, a value identical to that found for the stationary instability.

Finally, as for the stationary mode A, we investigate the physical interpretation of the oscillating adjoint global mode interpreted as the optimal initial perturbation. For a time $t = 0$, we reconstruct the linear superposition of the base flow q^0 and the adjoint global mode $\hat{q}_B^{1\dagger}$ with a finite amplitude ε. Similar to the stationary instability, $\varepsilon = 2.4 \times 10^{-2}$ for the disk and $\varepsilon = 4.9 \times 10^{-4}$ for the sphere, so that the maximum streamwise velocity perturbation represents 10% of the maximum streamwise velocity $w_{\max}^0$ in the case of the disk, and 1% in the case of the sphere. Fig. 12 shows the streamlines of the adjoint global mode in the region of the separation point in the azimuthal planes $\theta = 0$ and $\theta = \pi$ at time $t = 0$. The solid and dashed lines stand for the separation line of the base flow and of the total initial flow $q^0 + \varepsilon \hat{q}_{Br}^{1\dagger}$, respectively. Results are similar to that obtained for mode A. In the case of the disk, the optimal initial perturbation corresponds to a periodic tilting of the separation line around the fixed separation point. In the case of the sphere, it

corresponds to a displacement of the separation point along the sphere surface. Finally, it can be seen comparing Figs. 7(a) and 12(a), or Figs. 7(b) and 12(b), for instance, that for the same amount of perturbation, we obtain a larger deformation of the recirculation in the case of the oscillating instability, owing to the larger receptivity of the associated global modes.

4. Conclusion

In this study, we have investigated the linear dynamics of the steady axisymmetric flow past an axisymmetric body. Two cases, the disk and the sphere, modelling characteristic geometries of blunt and bluff bodies, have been considered. A linear global stability analysis has been carried out, whose results show good agreement with that of Natarajan and Acrivos (1993). A first instability occurs for a stationary global mode A of azimuthal wavenumber $m = 1$. The adjoint global mode A associated to this direct global mode has been computed and the physical effect of this optimal perturbation on the recirculation area is to modulate the separation angle around the disk edge or to displace the separation point along the sphere surface with no tilting of the separation line. The spatial separation of the direct and adjoint global modes has been interpreted as a result of the convective non-normality, resulting from the transport of the perturbations by the base flow. Downstream from the body, the direct global mode A is dominated by the streamwise velocity component and in the recirculating bubble, the adjoint global mode A is dominated by the cross-flow components, which suggests that a lift-up mechanism is involved in the energy production of the instability. A second instability occurs for an oscillating global mode B of azimuthal wavenumber $m = 1$. The associated adjoint global mode B has been computed and the physical effect on the recirculation area has been shown to be, as for mode A, a periodic rotation of the separation line at the disk edge or a periodic translation of the separation point along the sphere surface. For both bodies and both instabilities, a detailed analysis of the adjoint global modes has allowed to identify different regions of the flow that are of particular interest in the perspective of control. The recirculation area, more specifically the vicinity of the separation point, is where all global modes are most receptive to initial perturbations and forcing of azimuthal wavenumber $m = 1$. As discussed in Giannetti and Luchini (2007), considering the overlapping of the direct and adjoint global modes A and B, the wavemakers for the stationary and oscillating instabilities have been identified as being located in the core of the recirculation area, and the vicinity of the separation line, respectively. If control is considered, this analysis suggests different locations of the actuator depending on the control method. In the case of passive control acting through steady, axisymmetric modifications of the base flow, the actuator should be placed so as to modify the base flow in the wavemaker region, presently in the recirculating bubble, to obtain a large impact on the dynamics. In the case of active control by blowing and suction at the body wall, the adjoint pressure distributions show that maximum efficiency is achieved placing the actuator precisely at the rime on the upstream face of the disk, and upstream of the separation point for the sphere. However, in the case of the sphere, the receptivity is one order of magnitude larger and the region of receptivity is broad, so that one may achieve good efficiency by moving the position of the sphere actuator around the separation point. Finally, the magnitude of the adjoint pressure are higher for the oscillating mode B than for the stationary mode A. Therefore, one may expect that the control of the oscillating instability requires less energy to be introduced in the flow to achieve the same efficiency.

References

Achenbach, E., 1974. Vortex shedding from spheres. Journal of Fluid Mechanics 62, 209–221.
Barkley, D., Gomes, M., Henderson, R., 2002. Three-dimensional instability in flow over a backward-facing step. Journal of Fluid Mechanics 473, 167–190.
Berger, E., Scholz, D., Schumm, M., 1990. Coherent vortex structures in the wake of a sphere and a circular disk at rest and under forced vibrations. Journal of Fluids and Structures 4, 231–257.
Chomaz, J.-M., 2005. Global instabilities in spatially developing flows: non-normality and nonlinearity. Annual Review of Fluid Mechanics 37, 357–392.

Chomaz, J.-M., Huerre, P., Redekopp, L., 1990. The effect of nonlinearity and forcing on global modes. In: Coulet, P., Huerre, P. (Eds.), New Trends in Nonlinear Dynamics and Pattern-forming Phenomena: The Geometry of Nonequilibrium. NATO ASI Series B, vol. 237, Plenum, New York, pp. 259–274.

Davis, T.A., 2004. A column pre-ordering strategy for the unsymmetric-pattern multifrontal method. ACM Transactions on Mathematical Software 30 (2), 165–195.

Davis, T.A., Duff, I., 1997. An unsymmetric-pattern multifrontal method for sparse LU factorization. SIAM Journal on Matrix Analysis and Applications 18 (1), 140–158.

Ehrenstein, U., Gallaire, F., 2005. On two-dimensional temporal modes in spatially evolving open flows: the flat-plate boundary layer. Journal of Fluid Mechanics 536, 209–218.

Fabre, D., Auguste, F., Magnaudet, J., 2008. Bifurcations and symmetry breaking in the wake of axisymmetric bodies. Physics of Fluids 20 (5), 051702 1–4.

Fornberg, B., 1988. Steady viscous flow past a sphere at high Reynolds number. Journal of Fluid Mechanics 190, 471–489.

Fuchs, H., Mercker, E., Michel, U., 1979. Large-scale coherent structures in the wake of axisymmetric bodies. Journal of Fluid Mechanics 93, 185–207.

Giannetti, F., Luchini, P., 2007. Structural sensitivity of the first instability of the cylinder wake. Journal of Fluid Mechanics 581, 167–197.

Gumowski, K., Miedzik, J., Goujon-Durand, S., Jenffer, P., Wesfreid, J., 2008. Transition to a time-dependent state of fluid flow in the wake of a sphere. Physical Review E 77, 055308 1–4.

Johnson, T., Patel, V., 1999. Flow past a sphere up to a Reynolds number of 300. Journal of Fluid Mechanics 378, 19–70.

Marquet, O., Lombardi, M., Chomaz, J.-M., Sipp, D., Jacquin, L., 2009. Direct and adjoint global modes of a recirculation bubble: lift-up and convective non-normalities. Journal of Fluid Mechanics 622, 1–21.

Marquet, O., Sipp, D., Jacquin, L., 2008. Sensitivity analysis and passive control of the cylinder flow. Journal of Fluid Mechanics 615, 221–252.

Moffatt, H., 1964. Viscous and resistive eddies near a sharp corner. Journal of Fluid Mechanics 18, 1–18.

Natarajan, R., Acrivos, A., 1993. The instability of the steady flow past spheres and disks. Journal of Fluid Mechanics 254, 323–344.

Ormières, D., Provansal, M., 1998. Transition to turbulence in the wake of a sphere. Physical Review Letters 83, 80–83.

Pier, B., 2008. Local and global instabilities in the wake of a sphere. Journal of Fluid Mechanics 603, 39–61.

Schmid, P., Henningson, D., 2001. Stability and Transition in Shear Flows. Springer, New York.

Schmid, P., Henningson, D., 2002. On the stability of a falling liquid curtain. Journal of Fluid Mechanics 463, 163–171.

Sevilla, A., Martínez-Bazàn, C., 2004. Vortex shedding in high Reynolds number axisymmetric bluff-body wakes: local linear instability and global bleed control. Physics of Fluids 16 (9), 3460–3469.

Sipp, D., Lebedev, A., 2007. Global stability of base and mean flows: a general approach and its applications to cylinder and open cavity flows. Journal of Fluid Mechanics 593, 333–358.

Thompson, M., Leweke, T., Provansal, M., 2001. Kinematics and dynamics of sphere wake transition. Journal of Fluids and Structures 15, 575–585.